Organic Non-Wettable Superhydrophobic Fullerite Films

Rinku Saran, David Fox, Lei Zhai, and Debashis Chanda*

A long-standing quest in material science has been the development of non-wettable superhydrophobic films based on a single organic material, without the requirement of fluorination or silane treatment. Here, such films and coatings, which are developed using colloidal gels of fullerite C_{60} and C_{70} nanocrystals, are described. It is illustrated that despite the high surface energy of these van der Waals molecular crystals their gelation can create films having self-affine fractal surfaces with multiscale roughness. Water droplets on resulting surfaces of fullerite films bead like a pearl resting in a Fakir state with contact angle exceeding 150°. The films are extremely water repellent and non-wettable; when submerged in water they stay dry up to 3 h even at a water depth of two feet and exhibit the plastron effect. A series of experiments are presented to provide comprehensive inspection of water droplet dynamics on these films. These include rolling, bouncing, squeezing, freezing, melting, evaporating; along with acidic and alkaline tests. Non-wettable films of such materials are unique as fullerites get photosensitized instantaneously generating extremely high yields (≈100%) of singlet oxygen ($^1O_2$) that can destroy viruses and bacteria; thereby enabling their use in rheology, water purification, and medicinal devices.

1. Introduction

Solubility of a solid substance in liquids is a physical constant, a measure of the maximum amount of solid solute that a liquid solvent can hold to form a true homogeneous solution at a specific temperature. The solubility of molecular solids of close-caged hollow carbon molecules coined as the fullerenes (C_{60} and C_{70}) have been studied with an intense inquisitiveness. Primarily, because fullerenes are the only soluble form of carbon among many of its allotropes. They are also the largest molecules known to form and exist in space,[1] even detected in the planetary nebula Tc-1 which is more than six thousand light-years away.[2] It was expected that due to their unique symmetrically caged molecules with sp^2 carbons they would interact with solvents very differently, hence providing new insights about both kinetics and thermodynamics of solute-solvent interactions. Ruoff et al. conducted a detailed systematic study on solubility of fullerene C_{60} in a variety of solvents, and concluded that there exists no universal solvent property that alone can explain or even predict the solubility of C_{60}.[3] In addition, it was discovered that solubility of C_{60} has an anomalous temperature dependence;[4] dissolution of C_{60} is exothermic above room temperature and endothermic below. These results motivated experimental studies on fullerene C_{70} which also showed similar solubility behavior.[5] Ambiguity persists on the solubility of fullerenes, and there exists discrepancies in reported solubility data. High solubility is usually observed at room temperatures in solvents having high refractive indices, large molecular volumes, and dielectric constants close to four.[3] Depending on the solvent nature, solubility of C_{60} and C_{70} can vary up to several orders of magnitude. For example, solubility of C_{60} in its weak solvents (alcohols) like methanol is ≈0.01 mg mL^{-1} and in strong solvents (naphthalenes) such as 1-chloronaphthalene is ≈50 mg mL^{-1}.[3] When solutions of fullerenes dissolved in their strong solvents are interfaced with their weak solvents; the resulting liquid–liquid interface can create solid crystals of fullerenes (fullerites).[6] Crystals are principally conceived by reducing the solute solubility in a nearly saturated solution via interfacing it with a solvent in which solute is sparingly soluble—this results in supersaturation, which initiates nucleation (onset of phase separation) and subsequent growth of crystals. Though, the precise theory and mechanism of crystallization from supersaturated solutions remains unclear to date and is often debated.[7] In particular, nucleation pathways and the critical cluster size of molecules requisite for crystal growth.[8] This solubility difference driven approach often referred to as the antisolvent crystallization is employed extensively in pharmaceutical industries

Dr. R. Saran, Dr. D. Fox, Prof. L. Zhai, Prof. D. Chanda
NanoScience Technology Center
University of Central Florida
Orlando, FL 32826, USA
E-mail: debashis.chanda@ucf.edu
Dr. R. Saran, Prof. D. Chanda
CREOL
The College of Optics and Photonics
University of Central Florida
Orlando, FL 32816, USA
Dr. D. Fox
Department of Chemistry
University of Central Florida
Orlando, FL 32816, USA
Prof. L. Zhai
Department of Materials Science and Engineering
University of Central Florida
Orlando, FL 32816, USA
Prof. D. Chanda
Department of Physics
University of Central Florida
Orlando, FL 32816, USA

**ADVANCED
SCIENCE NEWS**
www.advancedsciencenews.com

**ADVANCED
MATERIALS**
www.advmat.de

for purification and separation processes; such a method is used to create a variety of nano-micro sized molecular structures including solvates, co-crystals, and polymorphs. Not only is purity considered in clinically regulated drugs that have been prepared as oral tablets, but the solubility and wettability parameters as well, which are vital to their function. These parameters may be tuned via control over crystal structure, size, and habit. Advanced versions of this technique to grow high purity fullerene crystals are also engendering significant interest with the demonstration of schemes to achieve control over crystal morphology, as elucidated in a recent report on nano-pottery of C_{60}.[9] Yet, high-throughput growth of fullerene crystallites, their utilization in schemes to develop solution processable films and subsequent use of films in potential applications remains unexplored; which we demonstrate in this work. Solution-cast fullerite films are of high importance considering their widespread use in organic optoelectronic devices as these materials are the best-known electron acceptors along with their high electron affinity and mobility. A majority of these applications make use of vacuum-sublimed C_{60} films whilst C_{70} remains a scarcely utilized material. Here, we first present a facile scheme to produce nanostructured solution-cast films of fullerene C_{60} and C_{70} from their colloidal gels. To this end, we make use of solubility difference driven crystallization principle to grow nano-sized fullerene crystals and the gelation of these crystals following centrifugal enrichment. Surface wetting characterization done via sessile droplet goniometry revealed that formation of films from such gels generates a superhydrophobic surface, and the resulting films as a whole are non-wettable.

Wettability is a surface property of solids, typically determined by the contact angle of a water droplet resting on its surface. The contact angle of such a water droplet can be used to determine several surface properties of the material. For example, contact angle of a water droplet on poly(tetrafluoroethylene) surface (Teflon) can approach a maximum of ≈116°. A solid surface is classified as superhydrophobic when contact angle exceeds 150°, the contact angle hysteresis is low and the wetting state (Cassie) demonstrates high stability. Such high contact angles (>120°) cannot be achieved by surface treatment or chemical functionalization; it is essential for the physical topography of the surface to be rough at nano-micrometer scale in such a way that its morphology may facilitate the entrapment of air underneath the droplet. This is revealed by examination of superhydrophobic surfaces of several plants and biological species which have naturally selected and adapted them over the evolutionary phases.[10] A classic example is the surface of *Nelumbo nucifera* (Indian lotus) leaf, formed of micrometer sized papillae with nanoscale branches coated with an intrinsic hydrophobic material (epicuticular wax). Fullerenes are hydrophobic molecules, fullerite solubility in water is estimated to be on the order of ≈10^{-10} ng mL^{-1}.[11] Vacuum-sublimed fullerite films, however, have not been observed to form superhydrophobic surfaces. Possibly, because sublimation precludes deposition of nanostructured films with surfaces that permits existence of a non-wetting topology. In fact, smooth surfaces of fullerites are hydrophilic in nature displaying a water droplet contact angle of 60°.[12] We find that if films are produced using colloidal gels, densely packed nano-structured rough surfaces are generated; such that the wetting behavior is dramatically

tuned from hydrophilic to superhydrophobic despite the fact that these materials have a high surface energy. Numerous superhydrophobic surfaces have been reported to date, reviewed recently.[13] Majority of them make use of inorganic materials or metals with few exceptions on multi-organic materials.[14] They are developed by creating a rough surface using either photolithography, chemical vapor deposition, self-assembly, or electrochemical etching; and typically require additional multi-fluorination or silane treatment.

Here, we show that a superhydrophobic surface with contact angle of ≈155° exhibiting non-wettability can be created simply by a drop of fullerite gels. We make use of self-affine fractal theory and apply wetting models to explain and examine the origin of non-wettability. Furthermore, we demonstrate underwater stability and plastron formations of the films that mimic hydrocarbon surface of alkali fly which survives in highly alkaline waters of California's Mono Lake. Artificial plastron formation and plastron recovery in situ, along with photo-induced chemical reactivity of C_{60} and C_{70} which can inactivate enveloped viruses makes these non-wettable films unique. Fullerite gels can be applied on any surface without requiring any additional process steps; and can be deployed directly for biochemistry, rheological experiments, and plethora of practical applications requiring hydrophobicity.

2. Results and Discussion

Nano-fullerites were grown via sonication coupled crystallization protocol. Herein, carbon disulfide (CS_2) was chosen as a common solvent for both fullerenes in which C_{60} and C_{70} have solubility of ≈7.9 and ≈9.8 mg mL^{-1}, respectively.[3,15] Dissolution of fullerene powders (30.5 mg) in CS_2 (5 mL) was carried out using a mini-vortexer operating at 2800 revolutions per minute (rpm) for 7 min. The resulting concentrated solutions (6.1 mg mL^{-1}) were then rapidly injected into glass vials containing isopropyl alcohol (10 mL), kept under continuous sonication at a frequency of 35 kHz. Isopropyl alcohol (IPA) here acts as an antisolvent in which both fullerenes have a low solubility of ≈2.1 µg mL^{-1}. The liquid–liquid interface (volume ratio 1:2) results in phase separation of fullerenes which is noticeable by the appearance of brown (C_{60}) and black (C_{70}) colloids. After 20 min of sonication more alcohol (5 mL) was added to colloidal solutions and vortexed for 3 min. Solutions were then left undisturbed for 15 min to allow the colloids to settle down, followed by decanting of the supernatant. This mixing and washing process was repeated several times until the supernatant appeared clear—redispersion left with a suspension of colloids (nano-fullerites). The photographs one-to-four presented in **Figure 1**a illustrates the entire growth protocol in sequence along with the resulting product obtained at each step. The transmission electron microscopy (TEM) and scanning electron microscopy (SEM) images of obtained nano-fullerites are presented in Figure 1b,c, respectively. Lattice fringes of C_{60} and C_{70} can be seen in high-resolution microscopy images revealing a highly ordered long-range molecular arrangement in both carbon crystallites, Figure 1b (middle). Reflection spots observed in the fast Fourier transform (FFT) pattern of the respective microscopy images represent the symmetry of respective lattice
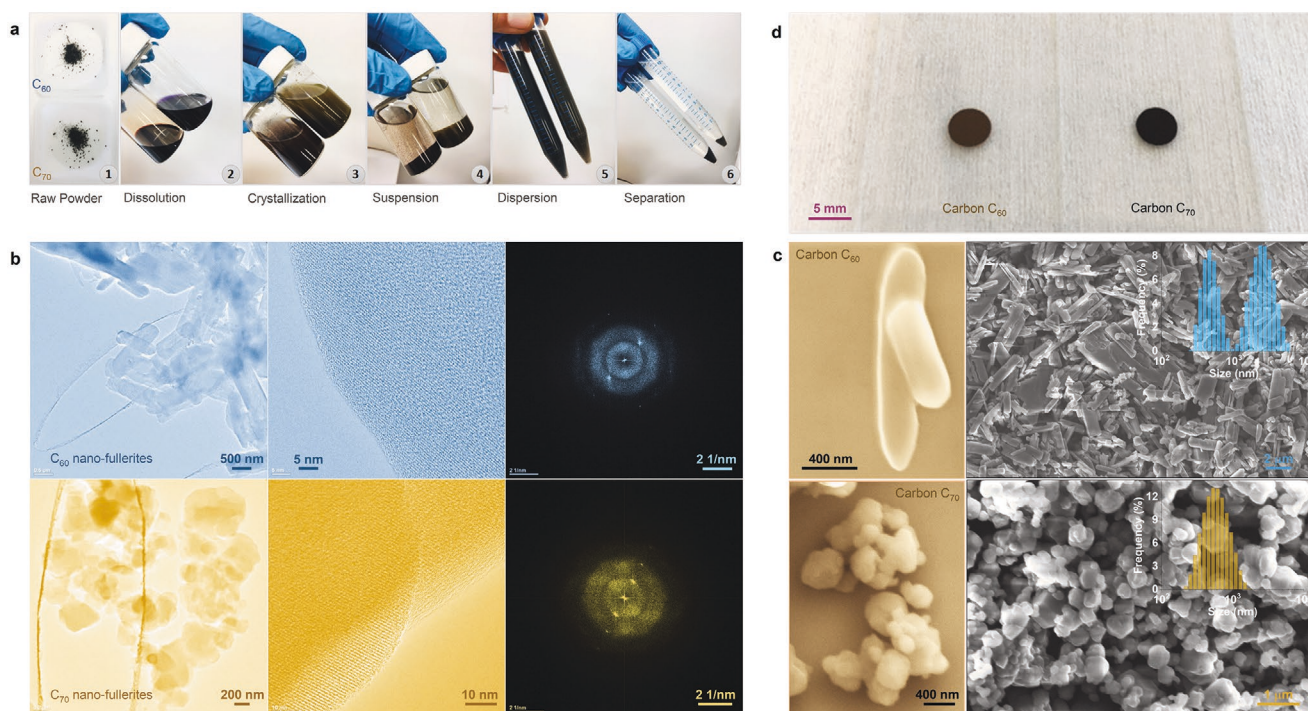
**ADVANCED
SCIENCE NEWS**

www.advancedsciencenews.com

**ADVANCED
MATERIALS**

www.advmat.de

Figure 1. Solution-cast C_{60} and C_{70} nano-fullerite films. a) Photographs in sequence illustrate a simple route to obtain high-purity fullerene nanocrystallites. Photograph one shows raw fullerene C_{60} and C_{70} powder which is dissolved in CS_2. Photograph two shows the resulting solutions of C_{60} (violet-purple color, top vial) and C_{70} (reddish-wine color, bottom vial), which were injected into IPA kept under ultrasonication. Photograph three shows the product obtained after the crystallization of fullerenes and sonication process. Photograph four shows suspensions of nano-fullerites after repeated washing with fresh IPA. Photograph five shows uniformly dispersed C_{60} and C_{70} colloidal solutions prepared for centrifugation. Photograph six shows nano-fullerites completely separated from the dispersant after centrifugation. This enrichment allows dense packing of nano-fullerites as a pellet—a prerequisite for their gelation. b) TEM images of C_{60} and C_{70} nano-fullerites (left). High-resolution microscopy images (middle) taken at the edges of C_{60} and C_{70} nano-fullerite revealing ordered lattice fringes and their respective FFT pattern (right). c) SEM images of C_{60} and C_{70} nano-fullerites. The inset to the microscopy images shows the size distribution profiles of C_{60} and C_{70} nano-fullerites. The magnified microscopy images display the typical crystal habit of C_{60} (elongated) and C_{70} (globular). d) Solution-cast C_{60} and C_{70} films deposited on glass slides from their colloidal gels. These films are superhydrophobic and non-wettable.

fringes, Figure 1b (right). As seen in the magnified SEM images (Figure 1c), C_{60} crystals exhibit an elongated/platy flat-bladed crystal habit whilst C_{70} crystallized in a globular/spherical habit. Insets to Figure 1c are the intensity weighted size distribution profiles of nano-fullerites measured via the dynamic light scattering technique. The Z-average was found to be ≈906.2 and ≈537.3 nm; and a polydispersity index of 0.44 and 0.12, for C_{60} and C_{70} respectively. To develop solution-cast films, well dispersed nano-fullerite solutions (1–1.5 mg mL^{-1}) were prepared following the washing process (photographs five, Figure 1a). These colloidal solutions were filled in conical-bottom centrifuge tubes and were subsequently centrifuged at 3000 rpm for 5 min. The centrifugal force separates nano-fullerite from dispersant enabling them to sediment at the bottom (pellet) of the tubes (photographs six, Figure 1a). The pellets were kept in tubes for a minimum of 3 weeks this allowed densely packed nano-fullerites to further agglomerate to gel. The photograph presented in Figure 1d shows few micrometer thin fullerene films of C_{60} and C_{70} deposited on glass slides via drop-cast from their colloidal gels. This solution-based scheme contrasts the conventional approach to produce fullerite films which are deposited by sublimation of fullerene powder (photograph one, Figure 1a) at high temperature (≈450 °C) under high-vacuum

conditions (≈10^{-6} Torr), thus offering an alternative route to produce nanostructured films. Large-area SEM images, additional TEM images, and a comparison of C_{60} and C_{70} dispersion stability are provided in Figures S1–S3, Supporting Information.

Surface chemical inspection of the films done via the X-ray photoelectron spectroscopy reveals presence of low intensity oxygen peak (O 1s) located at binding energy of ≈531.33 eV (C_{60}) and ≈531.2 eV (C_{70}) as films are prepared in air, Figure S4, Supporting Information. The carbon core line (C 1s) in both materials is symmetric and has a Gaussian nature with a full width at half maximum (FWHM) of ≈0.75 eV for C_{60} and ≈0.77 eV for C_{70} (resolution limited), **Figure 2**a,b. The core line of C_{60} is ≈280 meV shifted toward the higher binding energy relative to C_{70} peaking at ≈283.75 eV. For both carbon materials, the distinct energy positions of their camelback-like satellite features referenced to their C 1s core line can be seen in Figure 2a,b. The first prominent peak observed at binding energy of ≈1.85 eV (C_{60}) and ≈2.53 eV (C_{70}) are due to direct electron transition from the highest occupied band to the lowest unoccupied band.[16,17] Purity of the films is further probed via analyzing the infrared (IR) and Raman active frequencies of their vibrational modes. C_{60} molecule has icosahedral (I_h) point group symmetry (four IR active modes) and addition of
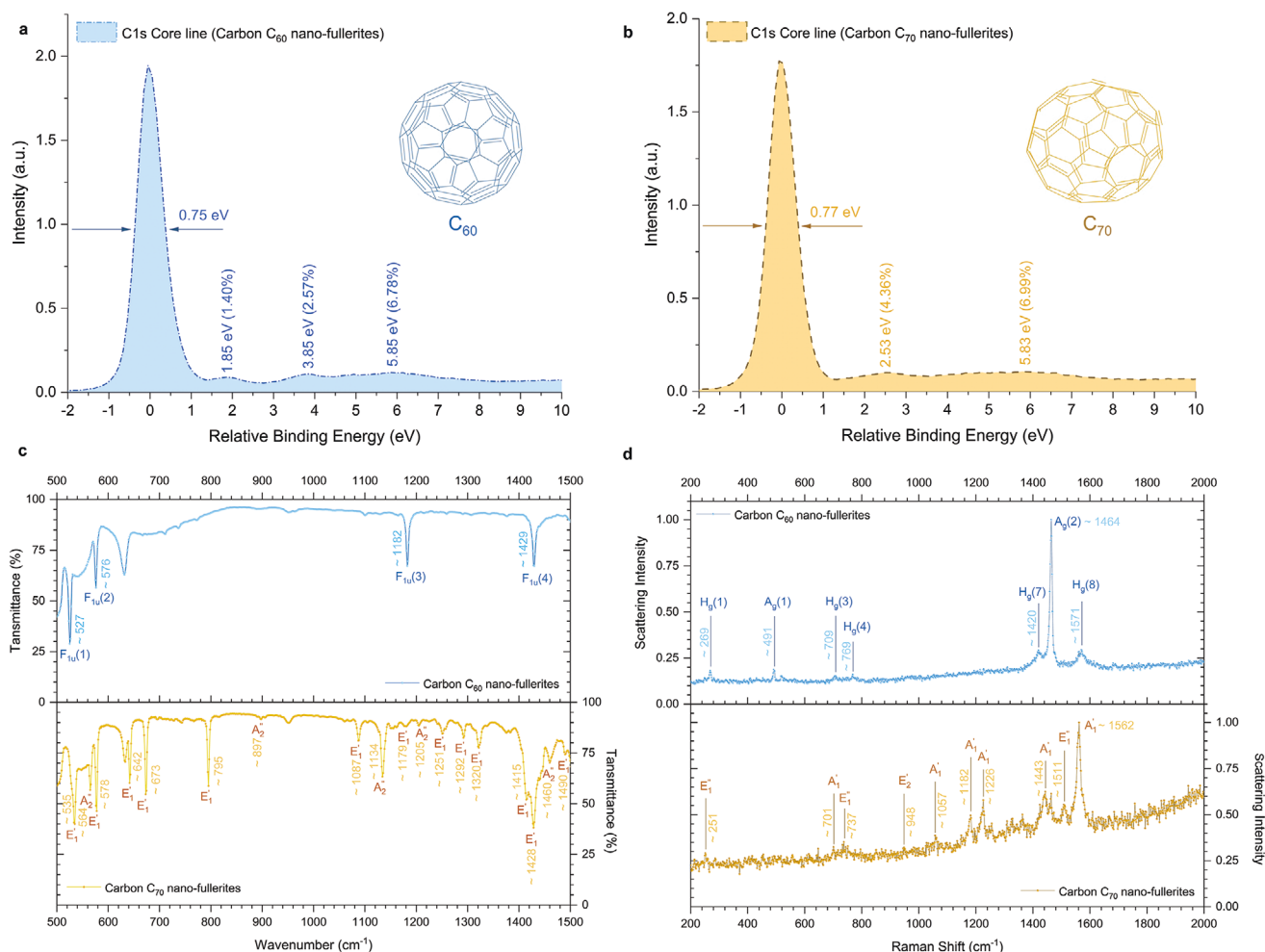
**ADVANCED
SCIENCE NEWS**

www.advancedsciencenews.com

**ADVANCED
MATERIALS**

www.advmat.de

Figure 2. Electronic and vibrational spectroscopy of C_{60} and C_{70} nano-fullerite films: a,b) Energy positions of camelback-like satellite features of both fullerenes referenced to their X-ray photoelectron C 1s main peak. First peak in both materials is due to direct electronic transition between bands. For C_{60} peak at ≈3.85 eV is attributed to dipole forbidden monopole like transition, followed by a peak at ≈5.85 eV due to dipole allowed π to π^* transitions. For C_{70} the peak at ≈5.83 is attributed to excitation of π plasmons. Inset to the respective figure is the molecular structure of C_{60} and C_{70}. The FWHM of C_{70} C1s line is observed 0.20 eV broader than that of C_{60} reflecting the five non-equivalent carbon atomic sites present in the ellipsoidal molecular structure of C_{70}. c) The FTIR spectrum of C_{60} (top) and C_{70} nano-fullerites (bottom). The peak appearing at ≈632 cm^{-1} in each spectrum is due to substrate absorption whose broad range (400 cm^{-1}–4000 cm^{-1}) spectrum is provided in Figure S5, Supporting Information. d) The Raman scattering spectrum of C_{60} (top) and C_{70} nano-fullerites (bottom) measured at an excitation wavelength of ≈514.5 nm. Vibrational peaks identified and assigned are highlighted by marking them in FTIR and Raman spectra.

ten carbon atoms lowers the symmetry of C_{70} molecule to (D_{5h}) symmetry [insets to Figure 2a,b], resulting in a higher number of vibrational frequencies (thirty-one modes). The Fourier-transform infrared (FTIR) absorption spectrum of C_{60} display all four modes associated with the radial [$F_{1u}(1)$ ≈527 cm^{-1} and $F_{1u}(2)$ ≈576 cm^{-1}], and with the tangential [$F_{1u}(3)$ ≈1182 cm^{-1} and $F_{1u}(4)$ ≈1429 cm^{-1}] motion of carbon atoms, Figure 2c. For C_{70}, within the frequency range of 500–1500 cm^{-1} eighteen peaks are identified. We have assigned these peaks based on previously calculated vibrational frequencies using density functional theory (DFT).[18] These include five A_2'' modes (564, 897, 1134, 1205, 1460 cm^{-1}) and thirteen E_1' modes (535, 578, 642, 673, 795, 1087, 1179, 1251, 1292, 1320, 1415, 1428, 1490 cm^{-1}), Figure 2c. The Raman active frequencies of C_{60} corresponding to the two A_g and five out of the eight H_g symmetries are observed in the scattering spectrum. The tangential "pentagonal pinch" mode

$A_g(2)$ ≈1464 cm^{-1} is most prominent and $A_g(1)$ radial "breathing mode" is noticed at frequency of ≈491 cm^{-1}, Figure 2d. The other Raman bands ≈269, ≈709, ≈769, ≈1420, ≈1571 cm^{-1} are assigned to $H_g(1)$, $H_g(3)$, $H_g(4)$, $H_g(7)$, $H_g(8)$ modes, respectively. C_{70} has fifty-three Raman active bands ($12A_1' + 22E_1' + 19E_1'$) and they all appear between the spectral range of 200–1600 cm^{-1}. We have only assigned ten notable peaks based on theoretical and simulated data reported previously.[19] These include six (A_1') bands [≈701, ≈1057, ≈1182, ≈1226.1, ≈1443.7, and ≈1562 cm^{-1}], one (E_2') band at ≈948 cm^{-1} and three (E_1') bands [≈251, ≈737, and ≈1511 cm^{-1}], Figure 2d. Electronic and vibrational spectroscopy indicates that molecular nature is preserved in nano-fullerites and they are essentially van der Waals bonded crystals. The broad-range FTIR spectrum, optical absorption spectrum, X-ray diffraction spectrum, and electrical characteristics of the films are provided in Figures S5–S8, Supporting Information.
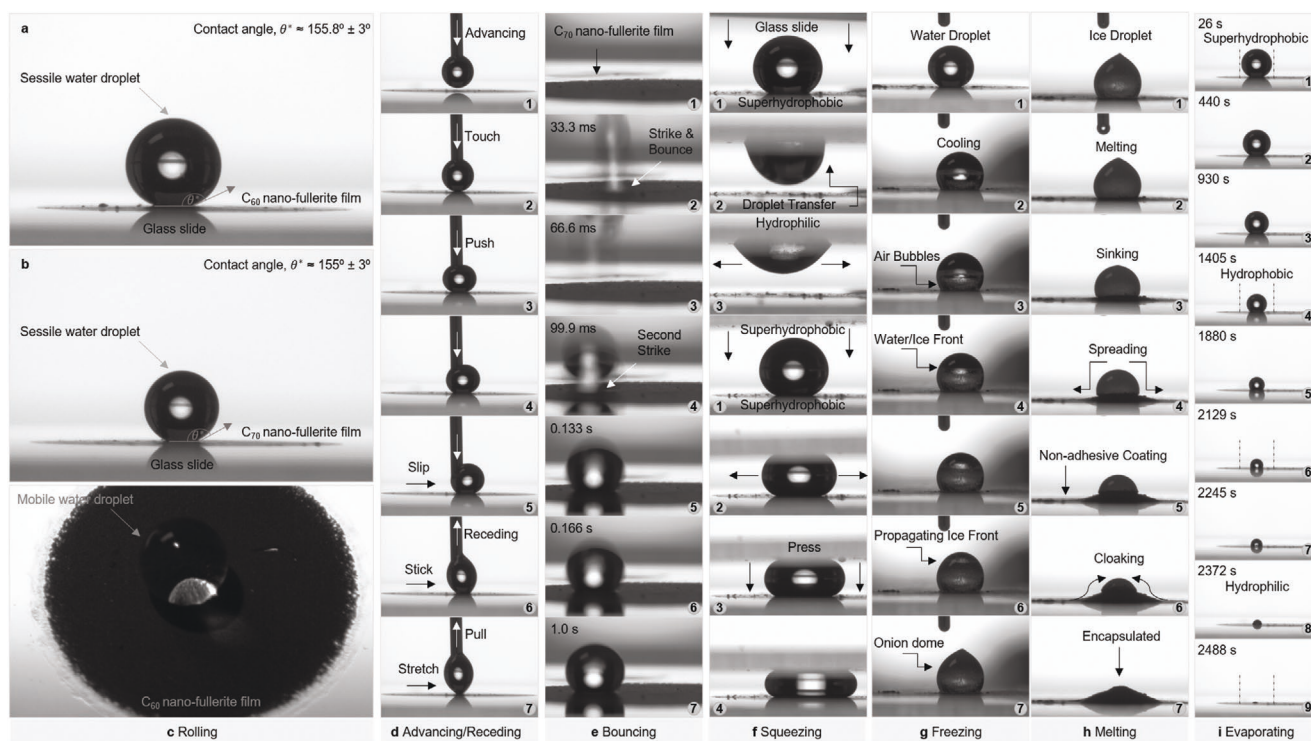
Figure 3. Surface wetting characterization and water droplet dynamics on C_{60} and C_{70} nano-fullerite films. a,b) 2D images are goniometry snapshots (side-view) showing a sessile water droplet on superhydrophobic surfaces of C_{60} and C_{70} films, respectively. c) Snapshot (top-view) of a water droplet rolling on a tilted C_{60} film (diameter ≈6 mm). The silver color seen at the droplet–surface interface is due to the plastron effect. d) Image sequence showing droplet–surface interface dynamics during advancing and receding movements of the needle with a droplet suspended at its front revealing a non-wetting interface. e) High-speed time frames of a water droplet bouncing on a C_{70} film. f) Sessile droplet on C_{70} deposit when interfaced with a hydrophilic glass surface is transferred without any loss of water (top image sequence, 1–3). Sessile droplet interfaced with another C_{70} deposit display extreme water repellency, even with the increase in pressure droplet remains squeezed between the surfaces without any impalement (bottom image sequence, 1–4). The droplet under this condition is observed to remain stable in its Cassie state for a period of 2 min and repeated press. g) Column sequence display supercooling of a sessile water droplet to freeze on a C_{70} film. h) Subsequent melting behavior of the droplet. The droplet is seen completely transferred to the underneath glass surface. i) Time lapse snapshots of an evaporation water droplet. The droplet maintains $\theta^* > 150°$ for ≈14 min during its lifecycle.

Unexpectedly, we notice that these nano-fullerite films exhibit superhydrophobicity. Using sessile droplet goniometry, we determined water droplet contact angles which typically remained ≈150° ± 6° even with variation in droplet volume and placement method. **Figure 3**a,b is the goniometry snapshots of a droplet resting on horizontally placed glass slides coated with C_{60} and C_{70} film displaying a contact angle of ≈155.8° and ≈155°, respectively. The error associated with contact angle measurement by manual baseline placement is ±3°. It should be noted that different mathematical models can be used for fitting the profile of a sessile droplet to determine the contact angle. These include circular, elliptical, tangent search, and Young–Laplace method. It is known that contact angle cannot exceed 156° under elliptical fitting,[20] which we have used. Other methods used for fitting provide contact angles in a similar range however, the use of Young–Laplace method provides contact angles approaching ≈170° for 3–5 µL droplets. When placed on a slightly tilted substrate (≈10°) droplets slide-off from the surface of these films. Droplets resting on the film can roll-off if the substrate is tilted leisurely. A snapshot of a droplet captured while rolling that appears like a pearl (top view) is shown in Figure 3c. (also, see Figure S9 and Movie S1, Supporting

Information). Experiments were undertaken to inspect the water droplet interface with C_{60} and C_{70} films, which revealed that the droplet does not make contact with their surface. In the image sequence shown in Figure 3d and Movie S2, Supporting Information, a droplet suspended from the needle is slowly advanced toward the film, and when it touches the surface does not detach from the needle. Advancing further downward, the droplet bulges and eventually moves away from its original position. As the needle is then gradually withdrawn, the droplet tends to stick to the surface and stretches. However, once sufficiently withdrawn completely detaches without wetting the surface. The time sequence images presented in Figure 3e shows water droplet can even bounce-off from the surface. Here, a droplet from the needle front fixed at a height of ≈3.5 cm from the film is released with soft vibration. Figure 3e shows droplet dynamics captured within 1 s. As the droplet contact time with the surface is extremely short, we were unable to captured dynamics shorter than ≈33 ms. However, a footprint of the first strike and bounce in a blurry motion can be seen, as well as a subsequent low bounce on second strike before the droplet comes to rest with a contact angle of ≈143°. The image sequence in Figure 3f and Movie S3, Supporting Information

**ADVANCED
SCIENCE NEWS**

www.advancedsciencenews.com

**ADVANCED
MATERIALS**

www.advmat.de

shows the droplet interface with two surfaces, an identical superhydrophobic surface (C_{70} deposit) and a hydrophilic surface (glass slide). As the glass slide is approached toward the droplet it instantaneously adheres to hydrophilic surface of glass and is completely transferred from the film without any loss of water, Figure 3f (top image sequence, 1–3). When the droplet is pressed with another C_{70} deposit, the droplet first moves between two surfaces as the initial force is applied on one side of the droplet, the contact angle hysteresis observed is less than 10°; with additional pressure the droplet starts to spread out and flatten, and can remain squeezed between both films without impalement, Figure 3f (bottom image sequence, 1–4). Upon release of the pressure droplet nearly regains its original profile (Movie S4, Supporting Information) or if further work is applied the droplet bursts. These observed behaviors during surface interface experiments are signature features of a superhydrophobic surface.

Wetting of solids is principally governed by their surface energy and surface roughness. Water has a surface tension of ≈73 mJ m^{-2}, its droplets are not able to spread fully on Teflon which has a low surface energy of ≈18 mJ m^{-2}, in comparison fullerites have an energy per unit area of ≈43 mJ m^{-2}.[12] On a chemically homogeneous and smooth surface, droplet spreading is decided by the sign of spreading parameter, $S = \gamma_{SG} - \gamma_{SL} - \gamma_{LG}$; where, γ_{SG}, γ_{SL}, γ_{LG} are the surface tension at the interface between solid–gas, solid–liquid, and liquid–gas respectively.[21] For $S \geq 0$ droplet spreads, complete wetting occurs with zero contact angle or otherwise ($\gamma_{SG} < \gamma_{SL} + \gamma_{LG}$) partial wetting will occur with a finite Young's contact angle (θ_Y) given by $\gamma_{LG}\cos\theta_Y = \gamma_{SG} - \gamma_{SL}$. For a smooth fullerite surface θ_Y is 60°. However, nano-fullerite films are observed to significantly amplify this angle (≈155° ± 3°) to an extent that droplets do not spread, instead beading up to have the appearance of a pearl. This unexpected enhancement in hydrophobicity is likely to originate due to the surface roughness of the films. To understand how surface roughness influences contact angle, Wenzel[22] and Cassie and Baxter[23] gave hypotheses supported by mathematical expressions. As per Wenzel, hydrophobicity is enhanced as roughness increases surface area, and the resulting change in contact angle is given by $\cos\theta^* = r\cos\theta_Y$ where, θ^* is apparent or the measured contact angle due to roughness factor r (ratio of actual to apparent surface area > 1). The use of the Wenzel model though is limited for $\theta_Y > 90°$, as for any values of $r > 1$ and $\theta_Y < 90°$ it predicts that roughness will promote wetting. The Cassie–Baxter model rests on the fact that rough surfaces entrap air, when a droplet is placed on them it sits on cushion of air (φ_g) contacting only the projected fraction of the solid surface (φ_s). On such a heterogeneous surface cosine of θ^* becomes weighted sum of contact angles of two homogeneous surfaces, air and the solid material as, $\cos\theta^* = -1 + \varphi_s(1 + \cos\theta_Y)$. Trapped air between film's surface and the droplet is visually seen during goniometry surface interface experiments (see Figure 3c and Movie S4, Supporting Information). The Cassie–Baxter expression is therefore modeled to determine φ_g and the relationship of measured θ^* up to theoretical maximum value of θ_Y, **Figure 4**a. As we see in the figure, for high percent values of φ_s the difference in θ^* is significant for low and high Young's contact angles. However, as φ_s reduces the band of θ_Y curves continue narrow approaching

the superhydrophobic zone. This indicates that the decrease in φ_s lessen the contribution of θ_Y or the materials surface energy. In fact, it diminishes the contribution of surface energy as this model predicts that $\theta^* \geq 150°$ can be obtained even for surfaces with $\theta_Y = 0°$ provided that $\varphi_s \leq 6\%$, however, for $\theta_Y = 120°$ this fraction is 20%. Fullerites (bold black curve) intersect with the vertical line on abscissa at measured $\theta^* \approx 155°$ providing ordinate value of $\varphi_s \approx 6\%$. Thus, the water droplets on the surfaces of the films rest on air (≈94%) in a Cassie or the Fakir state. It should be noted that surfaces of these films are not designed to achieve roughness with a low percent of φ_s. The traditional way to develop a superhydrophobic surface based on the Cassie–Baxter model involves design of a Fakir carpet—sub-micrometer level arrays of posts or pillars with well-defined geometry and intervals, surface roughness here is indeed definite and regular in all aspects. Such a single patterned structure usually made from high-surface-energy materials requires another coating of material with $\theta_Y > 90°$. In contrast, roughness resulting from drop-casted fullerite films is random and irregular and will vary for each deposit—despite that the resulting surface is still observed to be superhydrophobic. Therefore, to wholly explain superhydrophobic behavior of these films it is necessary to classify and characterize their surface roughness. An even more intriguing observation we made is that surface roughness resulting from assembly of freshly grown nano-fullerites (without centrifugation) or a deposit from fresh pellet (with centrifugation), both displays a completely opposite hydrophilic behavior. We found that nano-fullerite films display $\theta^* \approx 150°$ only if their pellets are "aged" over time.

The stark difference in wetting behavior of surfaces originates following centrifugation which essentially results in dense packing of nano-fullerites as a pellet. As nano-fullerites are kept in dispersant they are prone to form clusters, they can do so either via agglomeration (reversible) or aggregation (irreversible). The formation of clusters is not spontaneous but rather a time dependent process. Over time as the clusters grow their mass (number of nano-fullerites) and spatial dimension changes—they fill up available space until the volume occupied by clusters nearly equal to the total space. When this happens the pellet suddenly gels. We note that pellet must reach its gel point for films to display non-wettability. Otherwise, we experimentally demonstrate and discuss in detail in Note S1, Supporting Information (Figures S10–S15, Supporting Information) that surfaces of fresh pellet deposit or a nominally smooth surface of nano-fullerite films are hydrophilic and wettable. Once gelation is achieved it is not necessary to create films, surface of any random deposit from aged pellet results in $\theta^* \approx 150°$ as a non-wetting roughness becomes inherent in the surfaces of gelled agglomerates. This is advantageous as we will show later that these gels can be randomly deposited on any platform and can be scaled up as pastes to develop large area superhydrophobic coatings. In colloidal science such agglomerated clusters and gels are known to have a fractally rough surface.[24,25] Their fractal description is fundamentally important as the randomness of their surface roughness cannot be described by any geometrical shape and statistical description by conventional methods like root mean square roughness depends on scale of observation. To further investigate, if resulting surfaces are fractals; and to differentiate between surface roughness of
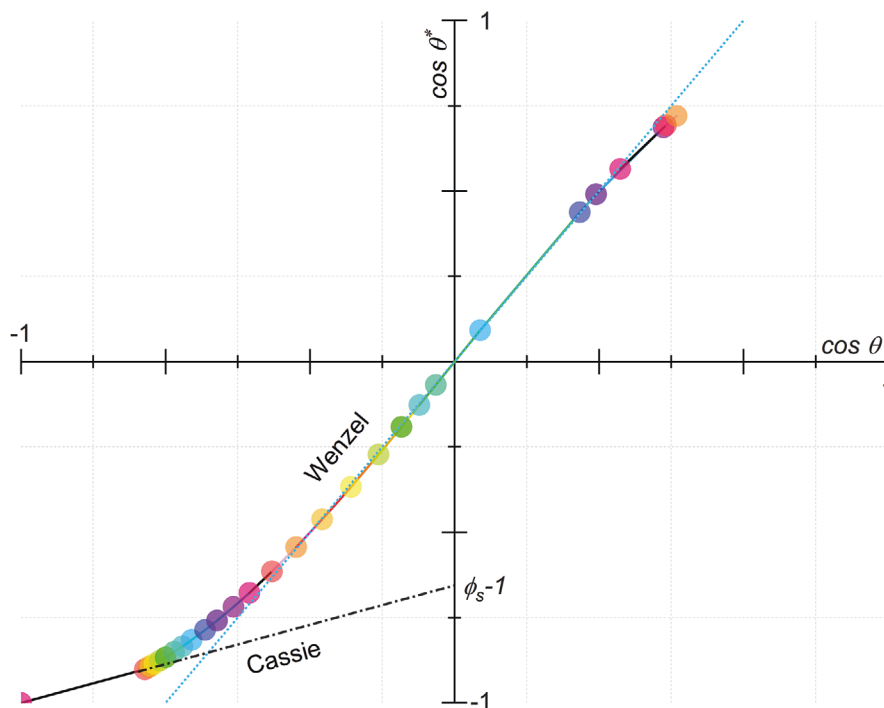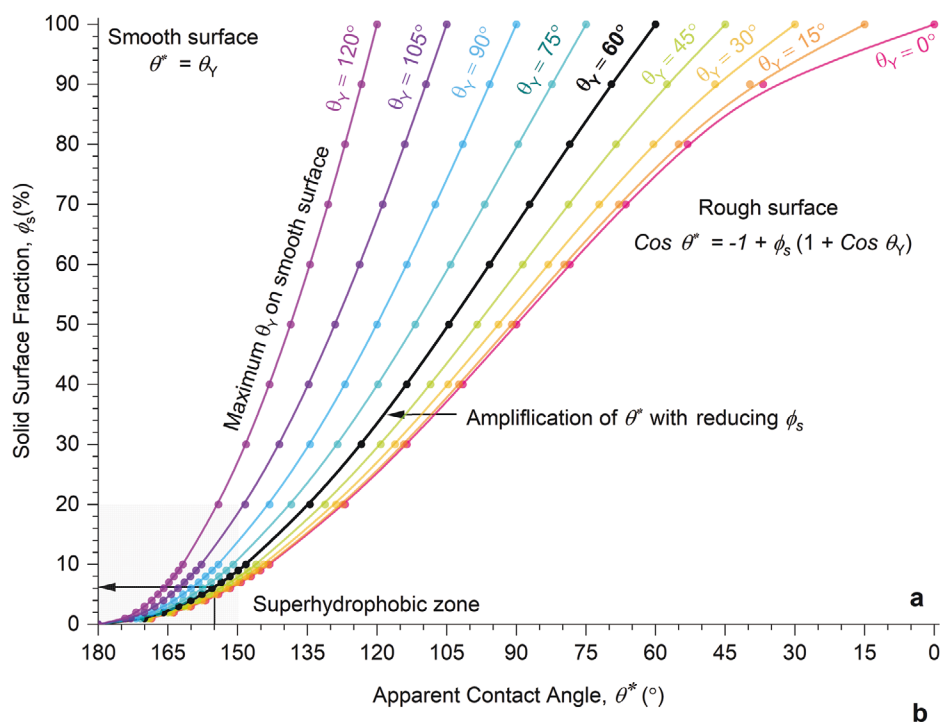
Figure 4. The Cassie model and wetting diagram: a) Modeled plot for an ideal Cassie droplet demonstrates relationship between solid surface fraction (φ_s) and apparent contact angle (θ^*) for typical values of materials intrinsic Young's contact angle (θ_Y). The parameter θ_Y is varied from 0° to 120° which the theoretical maximum possible angle on a smooth surface. The shaded region represents superhydrophobic zone ($\theta^* > 150°$). Model predicts that any rough surface providing $\varphi_s \leq 6\%$ can be made superhydrophobic, θ_Y or the materials surface energy is not essentially a limiting factor. The bold black curve represents smooth fullerite surface ($\theta_Y = 60°$) which approaches $\theta^* = 150°$ for $\varphi_s \approx 9\%$. For the measured $\theta^* \approx 155° \pm 3°$ water droplet only contact's ≈ 5–8% of the nano-fullerite surface. b) Wetting diagram shows change in apparent contact angle (θ^*) for an evaporating water droplet signifying how droplets wets the surface. The droplet maintains $\theta^* > 150°$ for ≈ 14 min in a Cassie state (black solid and dash-dot line) with a very low percent of φ_s. The fraction φ_s reduces with time as droplets starts to wet the surface, slowly making a transition to the Wenzel state. The blue dotted line crossing quadrant III to I represents the Wenzel model.

**ADVANCED
SCIENCE NEWS**

www.advancedsciencenews.com

**ADVANCED
MATERIALS**

www.advmat.de

wettable and non-wettable nano-fullerite films we acquired and analyzed their surface roughness power spectral density (PSD) plots. Roughness spectra were analyzed by fitting the fractal models (self-affine and K-correlations models). A complete description of surface roughness by fractal geometry and discussion on associated PSD is provided in Note S2, Supporting Information (Figures S16 and S17, Supporting Information). From the examination of PSD plots, we find that non-wettable surfaces have an increasing roughness amplitude (out-of-plane roughness) and enhanced correlation length (in-plane roughness). Furthermore, resulting surfaces are not perfect fractals, their power law behavior does not continue across all spatial frequencies instead representing two self-affine surfaces. Theoretically, it has been shown that it is not definite that fractal surfaces will induce non-wettability.[26] Only a certain class of self-affine fractal surfaces can induce non-wettability, even for material with $90° < \theta_Y > 0°$, if the asperities provide overhangs at least for the smallest indentations. Surface morphology inspection by high-resolution imaging at several magnifications revealed that surface formed of agglomerates of aged pellets have indentations with asperities at different scales of magnification (Figures S12 and S15, Supporting Information). We therefore conjecture that surfaces with self-affinity resulting from their gelation principally cause non-wettability of the films—essentially roughness is multiscale, consequence of which is that films trap air at several length scales and depths of its thickness. A gelled network of agglomerates not only provides but also cements this roughness. Air trapping is not only favored on these surfaces but also maintained. The deeper air pockets within the indentations are largely isolated so air does not have a single channel to escape. Hence, collectively surface develops a robust superhydrophobic roughness.

The effect of water droplet phase change on these superhydrophobic surfaces is examined by probing the dynamics of a supercooled water droplet and an evaporating water droplet. The column sequence in Figure 3g,h shows icing and subsequent melting behavior of a droplet. For freezing the droplet, a dry ice (solid carbon dioxide) cooled plate is placed underneath the glass slide. Soon after, the droplet loses its Cassie state making a transition to the Wenzel state (Movie S5, Supporting Information). As seen in Figure 3g base radius of the droplet changes and it is in contact with the surface. Following which isolated air bubbles start to appear in the droplet due to separation of air dissolved in water as the new solid phase of water cannot accommodate air in their crystal lattice. The density of bubbles increases as the ice front propagates upward; however, the rising velocity of the bubbles is slower than that of the propagating ice front so they get trapped during the solidification process. The freezing front advances upward leading to solidification in an onion dome-like shape (Movie S5, Supporting Information). The cold metal plate is then removed, and the frozen droplet is allowed to melt at room temperature. During melting, water penetrates the film and reaches the hydrophilic glass. This happens due to the droplet undergoing a Wenzel transition during freezing which facilitates water to fill the indentations and induce a pathway through the film to reach the substrate. Remarkably, film starts to cloak the sinking droplet and encapsulate it in its solid state (Movie S6, Supporting Information). The droplet can be seen fully transferred

and stored underneath the film on the glass surface, Figure 3h. Such a functionality cannot be achieved on a rigid nano-micro textured superhydrophobic surfaces. Time lapse images in Figure 3i shows sequence of an evaporating droplet under ambient condition. The droplet took ≈46 min to fully evaporate. Contact angles were measured as a function of time, which we have plotted in the wetting diagram (only $\theta*$) to identify different wetting regimes, Figure 4b. With an initial $\theta* ≈ 154.3°$, there is a gradual decrease in contact angle with time till it crosses from quadrant III to I to reach $\theta* ≈ 44°$. This decrease in $\theta*$ with time is attributed to simultaneous increase in the Laplace pressure $P = 2\gamma/R$, (γ is the surface tension of water) which impel water into the surface. As the water droplet slowly evaporates, its radius decreases over time and therefore its radius of curvature (R) leading to an increase in pressure which leads to sag in the indentations enabling water to contact the surface.[27] Once such nucleation points are established water can spread on the films slowly displacing air. In the wetting diagram transition (small bend) from the initial Cassie state to the Wenzel state (linear) can be seen. We find that the droplet maintains $\theta* > 150°$ for ≈14 min (Figure S18, Supporting Information), what is typically observed on designed Fakir carpets.[27]

Millimetric-sized water droplet on nano-fullerite films deposited simply as a drop of gel can rest on them without penetrating or spreading in superhydrophobic state, **Figure 5**a. These films are also observed to hold tiny droplet vertically and even when substrate is turned upside down (Figure S19, Supporting Information). To ascertain that films are non-wettable, we tested them under stationary and continuous flow of water over them from top and sides on a range of substrates (Movie S7, Supporting Information). Extreme water repellency is displayed by these films. The photograph presented in Figure 5b shows a nano-fullerite film deposited at the center of a nanostructured metallic surface (aluminum). The substrate placed in a Petri dish is subsequently filled with water. We see that film stops water at its outer periphery forming a cavity, although the level of water is several orders of magnitude higher than the thickness of the film. Similar observation can be seen under running water where film halts the flow of water, here deposited on a silicon wafer, Figure 5c. These films stay dry even when they are fully dipped in a pool of water repeatedly (Movie S7, Supporting Information). Superhydrophobic surfaces of many plant leaves and biological species display such non-wettability. As an example, here we show leaves of *Loropetalum chinense* (Chinese fringe). The photograph presented in Figure 5d shows several water droplets placed on the leaves of the plant. When a branch of this plant is immersed in water both adaxial and abaxial surfaces of its leaves appear like a glistening silver mirror, Figure 5e. The origin of silver appearance is a consequence of the total internal reflection occurring due to presence of air tapped between water and surface of leaves, collectively termed as the plastron effect (Figures S20, S21 and Movie S7, Supporting Information). We find that plastron on these leaves is not stable, repeated immersion or agitation results in loss of plastron. Few remarkable biological species like the *Ephydra hians* (Alkali fly) of California's Mono Lake forms highly stable plastron. Ancestors of this fly evolved in a very unique ecology. The water of Mono Lake is highly alkaline (pH 10), three times saltier than ocean water—no fish can survive here, the only other inhabitants found in
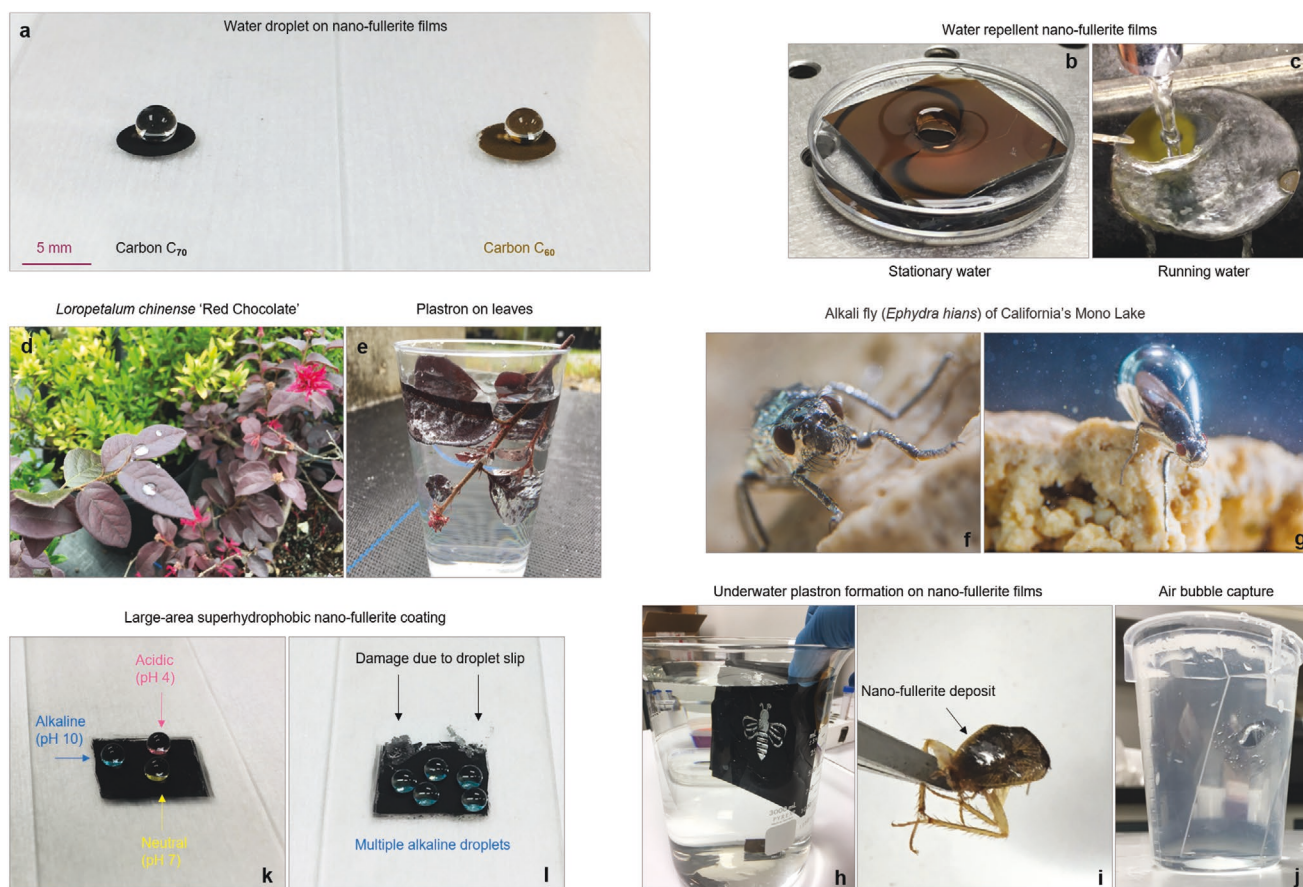
**ADVANCED
SCIENCE NEWS**

www.advancedsciencenews.com

**ADVANCED
MATERIALS**

www.advmat.de

Figure 5. Non-wettability and plastron effect: a) Millimetric sized water droplets placed on superhydrophobic surface of nano-fullerite films deposited on a hydrophilic glass slide. b) The photograph shows a C_{70} film (diameter ≈6 mm) deposited at the center of metallic substrate placed in a Petri dish. Water is poured from side to wet the surface; films display extreme resistance to wetting. c) C_{70} film deposited at the edge of silicon wafer; the film displays water repellency even under continuous running water flow. d) Photograph showing water droplets placed on the leaves of *Loropetalum chinense*. e) A branch of plant dipped in a glass of water. Leaves of this plant appear silver underwater due to the plastron effect. f,g) *Ephydra hians* of California's Mono Lake. This fly not only forms highly stable plastron covering its whole body except its eyes but can also trap air in the form of bubble underwater. f,g) Reproduced with permission: copyright Floris van Breugel/naturepl.com. h) Plastron effect displayed by C_{70} nano-fullerite deposited using colloidal gel that mimics superhydrophobic surfaces of plants and biological species. i) Colloidal gel deposited on the surface of a deceased cockroach displaying plastron effect underwater. j) Air bubble captured by C_{70} nano-fullerite film underwater imitating the air bubble formed by the alkali fly of Mono Lake. k,l) Large-area superhydrophobic coatings pasted using gels on glass slide (dimension ≈12.5 mm × 12.5 mm). As seen in the photographs these surfaces can even sustain multiple acidic and alkaline droplets.

lake are bacteria, algae, and tiny shrimp. However, the lake is home to trillions of alkali flies. To survive in the lake, they not only form a thin layer of plastron covering their face and legs but form a large air bubble around its superhydrophobic cuticle, Figure 5e,g. The fly uses the air bubble like a submarine, which enables it to crawl underwater up to 15 min at a water depth of few meters. Floris van Breugel and Michael H. Dickinson recently studied adaptation of the alkali fly to Mono Lake in detail.[28] They found that other six relatives of this fly do not have this capability and attributed this to the presence of relatively dense setae (tiny hairs) compared to other flies and presence cuticular hydrocarbons. Densely packed nano-structured surface as well as chemical similarities exist between fullerenes and hydrocarbons; both crystallize with van der Waals bond and are non-polar in nature, these factors enhance waterproofing.

We show that nano-fullerite films stay dry underwater by forming highly stable plastron when submerged, remaining

stable even when submerged in sodium carbonate (Na_2CO_3) rich solution with pH 10, mimicking the behavior of the alkali fly in the water of Mono Lake (see Movie S8, Supporting Information). The photograph presented in Figure 5h shows a black acrylite substrate dipped in water. Its surface masked with a honeybee stencil is coated using the colloidal gel. When viewed from certain glancing angles or rotated plastron effect is observed. The substrate was tested over a 3-month period, and the plastron was sustained without any degradation. To further show the applicability of gels we deposited them on a deceased cockroach that has a greasy surface (Figure S22, Supporting Information). When dipped in water where the deposit was thin comes off due to expansion of cockroach body parts however, the plastron can be seen where the deposit is sustained, Figure 5i. These demonstrations show the applicability and ease of which a non-wettable coating can be applied simply by depositing few drops of gels for their potential use in

underwater application that includes anti-biofouling, anti-corrosion, or to reduce frictional drag. Close inspection of plastron reveals that it is present either in the form of very thin layer of air or hemi-wicking blisters depending on the surface morphology underneath. Regardless, it completely covers random deposits or films protecting them underwater. It is possible to inject or trap additional air bubbles into plastron that can remain stored underwater in the form of large blister (volume ≈ 0.25 cm^3), Figure 5i. The stored air can be replenished repeatedly with the films retaining their thin plastron layer (Movie S9, Supporting Information). We emphasize that aqueous media applications of these surfaces are more attractive as they are superaerophilic underwater. For example, to capture undesired bubbles in a microfluidic channel or bubble capture during a leak of flammable gas. Furthermore, fullerenes are known to inactivate enveloped viruses in biological aqueous systems.[29] In the presence of visible light and oxygen, fullerenes instantaneously get photosensitized generating extremely high yields of singlet oxygen ($^1O_2$). This form of oxygen is highly cytotoxic, which can destroy proteins and DNA and is a well-established methodology for killing cancer cells referred to as photodynamic therapy. In such superhydrophobic photosensitizer applications amount of oxygen present in fullerites measured by XPS is highly beneficial. We further tested plastron stability at a water depth of 2 feet, with the film displaying plastron up to a maximum of 3 h (Figure S23, Supporting Information). The plastron then decays slowly over time with films appearing greyish in color, which may occur due to dissolution of trapped air in water. However, plastron can be regenerated in situ simply by injection of air onto the submerged films (Movie S10, Supporting Information). Finally, we demonstrate that colloidal gels can be scaled to create large-area surface coatings. Figure 5k,l shows large-area superhydrophobic surface created by drop casting gel and scaling them as paste using a glass pipette. To test the chemical stability of these surfaces, we used acidic (pH 4), neutral (pH 7), and alkaline (pH 10) droplets, Figure 5k. As seen in the Figure 5l the surface can also sustain multiple droplets. Both acidic and alkaline solutions were found to erode the coatings if a droplet slips to edges of coating, Figure 5l. In particular, if they are deposited on glass, however they adhere well on a silicon surface. Mechanical stability and durability of all superhydrophobic coatings have been a major concern since all surfaces are susceptible to abrasion when used for real world applications. To circumvent this issue, a new design strategy is reported very recently which is receiving significant attention.[30] It involves the use of an armored microstructure that contains pockets that can be filled with water repellent fragile nanostructures. These surfaces were demonstrated by incorporating fluorinated nanoclusters of silica and the resulting surfaces were found to preserve superhydrophobocity even following repeated abrasion from a sharp steel blade. Gelled nanofullerite clusters are well suited for such microstructures that can house them to provide extreme robustness.

3. Conclusion

We have presented a simple method to produce solution-cast fullerite films using colloidal gels. Gelation is achieved via

nanocrystallization of fullerenes, subsequent enrichment, and aging. We found that films prepared using gels create a superhydrophobic surface, despite high surface energy of these materials. However, surfaces resulting from assembly of freshly prepared nano-fullerites and their smooth films both were found to be hydrophilic. Superhydrophobic surface developed on inherently hydrophilic metals using femtosecond laser irradiation are well-known.[31–33] The randomness of non-wetting surface roughness is characterized via the self-affine fractal models and was distinguishable from the wettable surface using the PSD plots. We have performed several experiments describing the water droplet behavior on these surfaces, demonstrated scalability of gels for large-area coatings and their chemical stability toward acidic and alkaline solutions. Furthermore, we showed that these films are non-wettable, they stay dry even when submerged two feet underwater by forming highly stable plastron that can be used for capturing and storing gases underwater. The use of plastrons and superhydrophobic surfaces has so far been limited for water repellency applications since they are usually developed using inorganic materials or metals with a hydrophobic topping that does not possess additional functional properties like the fullerene materials. We anticipate these fullerite films coupled with their non-wetting properties can be exploited in many experiments and applications which were previously not possible. As both C_{60} and C_{70} are highly reactive species of carbon; well known for their use in water splitting electrocatalysis, bacterial disinfection, hydrogen generation, as an electron acceptor, and antioxidant along with their high electrochemical stability. In this context, the findings presented in this article will serve as a reference point for future development of these pure organic non-wettable superhydrophobic films.

4. Experimental Section

Fullerene powders (C$_{60}$ sublimed 99.9% Beantown Chemical Corporation, USA) and (C$_{70}$ 99%, Beantown Chemical Corporation), IPA (≥99.5%, VWR Chemicals BDH) carbon disulfide (anhydrous ≥99%, Sigma Aldrich), and pH buffer solutions (Thermo Scientific) were used as received. Antisolvent crystallization was used to grow fullerites. Factors that determined growth and shape of fullerites were discussed in detail elsewhere.[34,35] A ZEISS Ultra-55 scanning electron microscope was used of imaging operated at an accelerating voltage of 5 kV. A JEOL-1011 transmission microscope was used of TEM imaging. Samples were prepared on a carbon grid. A Malvern Panalytical's Zetasizer Nano ZS90 operating at 633 nm was used for measuring the size distribution via dynamic light scattering technique. Dilute colloid solutions of nano-fullerites dispersed in IPA were prepared in disposable plastic cuvette for measurements. A Physical Electronics 5400 ESCA was used for X-ray photoelectron spectroscopy. A Shimadzu IRSpirit Fourier transform infrared spectrophotometer was used for transmittance measurements. A Renishaw RM 1000B Micro-Raman spectrometer was used for acquiring the Raman spectra. The optical absorption spectra of the films were measured using a Cary 500 UV–vis-NIR spectrophotometer. The electrical characteristics of the films were measured using a Keithley 2400 source meter. Surface wetting characterization was carried out using a goniometer (DataPhysics). In a typical experiment, circular films of diameter ≈5 mm were deposited on glass slides and dried using nitrogen blow. Millimeter-sized droplets (volume ≈ 3–6 μL) were placed on the films either gently from the dispensing system and were video recorded using a high-speed camera. The frames of the video (after the droplet achieve equilibrium state on the surface ≈30 s) were

then analyzed to determine the water droplet contact angles via fitting the droplet profile using the elliptical method with baseline placed manually. The commercially available software package Gwyddion was used to obtain the PSD via analysis of surface SEM images, on the assumption that resulting numerical results and statistical information was independent of pixel resolution and particular scan size; and error associated the way in which software computed data. ImageJ software was used to obtain the 3D surface profile plots and line scans via image analysis.

Supporting Information

Supporting Information is available from the Wiley Online Library or from the author.

Acknowledgements

Conflict of Interest

The authors declare no conflict of interest.

Data Availability Statement

The data that support the findings of this study are available from the corresponding author upon reasonable request.

Keywords

[1] O. Berné, A. G. G. M. Tielens, *Proc. Natl. Acad. Sci. USA* **2012**, *109*, 401.

[2] J. Cami, J. Bernard-Salas, E. Peeters, S. E. Malek, *Science* **2010**, *329*, 1180.

[3] R. S. Ruoff, D. S. Tse, R. Malhotra, D. C. Lorents, *J. Phys. Chem.* **1993**, *97*, 3379.

[4] R. S. Ruoff, R. Malhotra, D. L. Huestis, D. S. Tse, D. C. Lorents, *Nature* **1993**, *362*, 140.

[5] R. J. Doome, S. Dermaut, A. Fonseca, M. Hammida, J. B. Nagy, *Fullerene Sci. Technol.* **1997**, 51593.

[6] K. Miyazawa, A. Obayashi, M. Kuwabara, *J. Am. Ceram. Soc.* **2001**, *84*, 3037.

[7] R. E. Schreiber, L. Houben, S. G. Wolf, G. Leitus, Z.-L. Lang, J. J. Carbó, J. M. Poblet, R. Neumann, *Nat. Chem.* **2017**, *9*, 369.

[8] J. F. Lutsko, *Sci. Adv.* **2019**, *5*, eaav7399.

[9] F. Han, R. Wang, Y. Feng, S. Wang, L. Liu, X. Li, Y. Han, H. Chen, *Nat. Commun.* **2019**, *10*, 1548.

[10] W. Barthlott, C. Neinhuis, *Planta* **1997**, *202*, 1.

[11] D. Heymann, *Fullerene Sci. Technol.* **1996**, *4*, 509.

[12] X. Ma, B. Wigington, D. Bouchard, *Langmuir* **2010**, *26*, 11886.

[13] S. Parvate, P. Dixit, S. Chattopadhyay, *J. Phys. Chem. B* **2020**, *124*, 1323.

[14] C. Peng, Z. Chen, M. K. Tiwari, *Nat. Mater.* **2018**, *17*, 355.

[15] N. Sivaraman, R. Dhamodaran, I. Kaliappan, T. G. Srinivasan, P. R. P. Vasudeva Rao, C. K. C. Mathews, *Fullerene Sci. Technol.* **1994**, *2*, 233.

[16] J. H. Weaver, J. L. Martins, T. Komeda, Y. Chen, T. R. Ohno, G. H. Kroll, N. Troullier, R. E. Haufler, R. E. Smalley, *Phys. Rev. Lett.* **1991**, *66*, 1741.

[17] B. Han, L. Yu, K. Hevesi, G. Gensterblum, P. Rudolf, J. Pireaux, P. A. Thiry, R. Caudano, P. Lambin, A. A. Lucas, *Phys. Rev. B* **1995**, *51*, 7179.

[18] V. Schettino, M. Pagliai, G. Cardini, *J. Phys. Chem. A* **2002**, *106*, 1815.

[19] G. Sun, M. Kertesz, *J. Phys. Chem. A* **2002**, *106*, 6381.

[20] X. Zhang, F. Shi, J. Niu, Y. Jiang, Z. Wang, *J. Mater. Chem.* **2008**, *18*, 621.

[21] D. Quéré, *Annu. Rev. Mater. Res.* **2008**, *38*, 71.

[22] R. N. Wenzel, *Ind. Eng. Chem.* **1936**, *28*, 988.

[23] A. B. D. Cassie, S. Baxter, *Trans. Faraday Soc.* **1944**, *40*, 546.

[24] S. Lazzaria, L. Nicoud, B. Jaquet, M. Lattuadac, M. Morbidelli, *Adv. Colloid Interface Sci.* **2016**, *235*, 1.

[25] J. Teixeira, *J. Appl. Crystallogr.* **1988**, *21*, 781.

[26] S. Herminghaus, *Europhys. Lett.* **2000**, *52*, 165.

[27] P. Papadopoulos, L. Mammen, X. Deng, D. Vollmer, H.-J. Butt, *Proc. Natl. Acad. Sci. USA* **2013**, *110*, 3254.

[28] F. van Breugel, M. H. Dickinson, *Proc. Natl. Acad. Sci. USA* **2017**, *114*, 13483.

[29] F. Käsermann, C. Kempf, *Rev. Med. Virol.* **1998**, *8*, 143.

[30] D. Wang, Q. Sun, M. J. Hokkanen, C. Zhang, F.-Y. Lin, Q. Liu, S.-P. Zhu, T. Zhou, Q. Chang, B. He, Q. Zhou, L. Chen, Z. Wang, R. H. A. Ras, X. Deng, *Nature* **2020**, *582*, 55.

[31] A.-M. Kietzig, S. G. Hatzikiriakos, P. Englezos, *Langmuir* **2009**, *25*, 4821.

[32] A.-M. Kietzig, M. N. Mirvakili, S. Kamal, P. Englezos, S. G. Hatzikiriakos, *J. Adhes. Sci. Technol.* **2011**, *25*, 2789.

[33] E. Bormashenko, T. Stein, G. Whyman, Y. Bormashenko, R. Pogreb, *Langmuir* **2006**, *22*, 9982.

[34] M. Sathish, K. Miyazawa, J. P. Hill, K. Ariga, *J. Am. Chem. Soc.* **2009**, *131*, 6372.

[35] J. Geng, W. Zhou, P. Skelton, W. Yue, I. A. Kinloch, A. H. Windle, B. F. G. Johnson, *J. Am. Chem. Soc.* **2008**, *130*, 2527.